A Study of Inertia-Gravity Waves in the Middle Stratosphere Based on Intensive Radiosonde Observations

Satoshi TATENO and Kaoru SATO

Department of Earth and Planetary Science, The University of Tokyo, Tokyo, Japan

(*Manuscript received 20 August 2007, in final form 14 June 2008*)

Abstract

An intensive observation of the stratosphere has been made using 10 radiosondes every 3 h for the time period of 11–12 May 2006 at Shigaraki, Japan (34.85°N, 136.11°E). Horizontal wind and temperature data were successfully obtained with high accuracy in the height region up to about 36 km. The sampling time intervals are 2 s corresponding to a nominal vertical resolution of about 10 m.

Two packets of wavelike fluctuations whose phases propagate downward are detected around a height of 34 km (hereafter referred to as Wave-A) and of 24 km (Wave-B) in the obtained vertical profiles of horizontal winds. Wave parameters are estimated using a hodograph analysis under an assumption that these fluctuations are due to inertia-gravity waves (IGWs). The ground-based wave periods are 11 and 21 h, the horizontal wavelengths are 850 and 900 km, and the vertical wavelengths are 6.0 and 2.6 km, for Wave-A and Wave-B, respectively. It is also shown that both IGWs propagate energy upward and north-northwestward relative to the background wind. The validity of the assumption is confirmed by the accordance of two independent estimates of the ground-based frequency. The horizontal structure seen in the horizontal divergence field calculated from European Centre for Medium-rangeWeather Forecasts (ECMWF) operational analysis data is consistent with the estimated wave parameters.

Sources of the two IGWs are examined by a ray tracing method. Both IGW rays are traced back to the level and latitude of the mid-latitude westerly jet. Detailed examination for temporal variation of the wave structure indicates that the IGWs meandered eastward slightly south of the mid-latitude jet, turned north-northwestward, ascended rapidly where the background wind direction was changed to southward, and reached the middle stratosphere over the observation site. An interesting point is that both locally-defined Rossby number and cross-stream Lagrangian Rossby number are large in the regions where the IGW packets were situated during propagation around the jet from several days. Therefore, it is likely that the IGWs were generated in the vicinity of the unbalanced westerly jet through the spontaneous adjustment processes.

1. Introduction

Through a lot of efforts in the last two decades using advanced observational tools such as Mesosphere-Stratosphere-Troposphere (MST) radars, lidars, radiosondes, and satellites as well as regional and global numerical models with fine spatial and time resolutions, our knowledge of internal gravity waves in the atmosphere has greatly improved (see a review by Fritts and Alexander 2003). It is now widely recognized that gravity waves play a significant role in the atmosphere through their ability to transport momentum. The gravity wave induced force is essential to drive the meridional circulation affecting the thermal structure in the middle atmosphere in the middle and high latitudes (e.g., Haynes et al. 1991; Plumb 2002) , and the oscillations of mean zonal winds in the equatorial atmosphere such as the quasi-biennial and

Corresponding author: Satoshi Tateno, Department of Earth and Planetary Science, The University of Tokyo, Tokyo 113-0033, Japan.
E-mail: tateno@eps.s.u-tokyo.ac.jp

semi-annual oscillations (e.g., Sato and Dunkerton 1997; Baldwin et al. 2001). Recent studies indicate another interesting role of gravity waves in the polar atmosphere. The temperature fluctuations of gravity waves affect the formation of polar stratospheric clouds controlling the ozone chemistry (e.g., Shibata et al. 2003; Watanabe et al. 2006).

Gravity waves are generated from various sources such as topography, convection, fronts, cyclones, and jet streams, mostly in the troposphere. Among these, the mechanism of spontaneous generation in the interior of the atmosphere has not been fully examined yet, although several observational studies show the existence of inertia-gravity waves (IGWs) with large amplitudes associated with the jet-frontal systems (Uccellini and Koch 1987; Sato 1994; Guest et al. 2000; Yamamori and Sato 2006). Recent numerical studies indicate that IGWs appear in the jet-exit regions (O'Sullivan and Dunkerton 1995; Zhang 2004; Plougonven and Snyder 2007). Since a locally defined Rossby number is large near the jet-exit regions, the simulated IGWs are considered to be generated by the so-called "geostrophic adjustment" (recently, the "spontaneous adjustment" is regarded as more appropriate terminology, because it is not proved that the flow is adjusted to the geostrophic balance, and because the geostrophic adjustment is usually treated as theoretical problems with unrealistic initial conditions). The IGWs are spontaneously generated even in the stratosphere near the polar night jet stream (Sato et al. 1999; Yoshiki et al. 2004; Sato and Yoshiki 2008). However, detailed characteristics of spontaneously emitted gravity waves such as momentum fluxes and phase velocities have not been well demonstrated theoretically so far. Accumulation of observations is, therefore, still needed for various height and latitude regions.

In this study, we have performed an intensive radiosonde observation in May 2006 at the site of the middle and upper atmosphere (MU) radar, which is an MST radar, in Shigaraki, Japan (34.85°N, 136.11°E). Wind and temperature data were successfully obtained in the height region up to about 36 km, allowing us to examine gravity waves in the middle stratosphere. This study is an extension of the statistical study made by Sato (1994) using observational data from the MU radar over three years. She inferred from group velocities estimated by a hodograph analysis that the IGWs observed in winter (defined as October through May) are originated from the middle latitude jet and topography, and that those in summer (defined as June through September) are originated somewhere in the lower latitudes. Oshima (1997) confirmed her inference by a ray tracing analysis (Marks and Eckermann 1995) using the wave parameters estimated by Sato. The height region of the MU radar observation is, however, limited up to about 22 km in the lower stratosphere, although MST radars providing accurate momentum flux estimates are an ideal observational tool to examine gravity wave effects on the mean flow. In our radiosonde observations, two interesting gravity wave packets were detected above the 22 km height in the middle stratosphere. This study reports detailed characteristics of the gravity waves that are estimated through a hodograph analysis. The wave sources and possible generation mechanisms are also examined by a ray tracing analysis method.

Details of the observations are described in Section 2. Results of the hodograph analysis are shown in Section 3. A ray tracing analysis is made in Section 4. Results are examined in Section 5 in terms of possible sources and propagation mechanisms. Summary and concluding remarks are made in Section 6.

2. Data description and background fields

Stratospheric observations were performed using 10 radiosondes (Vaisala RS92) from 1500 LST (0600 UTC) 11 May 2006, to 1800 LST 12 May 2006 at Shigaraki, Japan (370 m elevation) at a time interval of 3 h. Vertical profiles were obtained for atmospheric pressure, temperature, relative humidity, horizontal wind direction and speed with sampling intervals of 2 s, corresponding to a nominal vertical resolution of about 10 m. Geopotential heights were obtained from pressure and temperature data assuming the hydrostatic balance. The data were linearly interpolated with a vertical interval of 10 m to make further analysis easier. Accuracy of wind data is about 0.2 m s^{-1}. Balloons attained a maximum altitude of 36 km on average before bursting, which allows us to examine gravity waves in the middle stratosphere. Heights are described relative to the ground in this paper.

Six-hourly ECMWF operational analysis data at 21 pressure levels from 1000 to 1 hPa were used to examine the large-scale structure of the background atmosphere. By examining geopotential height fields at 10 hPa, it was found that the stratospheric polar vortex breaking occurred in early May and that an anticyclone was formed over the

Arctic in late May (not shown). The zonal mean zonal wind at a 10-hPa pressure level decreased gradually from March to June, and converted from westerly to easterly in early May in 2006. Thus, our observation period corresponds to the transition period from winter to summer in the stratosphere.

Figure 1 shows time series of vertical profiles of observed zonal and meridional winds. A peak corresponding to the mid-latitude westerly jet is located around a height of 14 km and a weak wind layer is observed around 23 km. A westerly wind maximum around 30 km in the period from 2100 LST 11 through 1200 LST 12 May is due to a cyclonic vortex situated to the north of Japan which was formed as a fragment of the breaking polar vortex.

A wavelike structure with a vertical wavelength of about 6 km is clearly seen around 34 km in the vertical profiles of meridional winds at 1500, 1800 and 2100 LST 11 May as denoted by a dashed line in Fig. 1 (Wave-A). The downward phase speed is about 0.12 m s^{-1} , and the groundbased wave period is about 13 h. Another clear wavelike structure with vertical wavelengths of 2–3 km and groundbased wave periods of 17–24 h is seen around a height of 24 km at 1200, 1500 and 1800 LST 12 May (Wave-B).

Wave-B components were extracted using a band-pass filter with cutoff wavelengths of 1.5 and 4.5 km from the vertical profiles of zonal and meridional winds for the three observations. On the other hand, a band-pass filter was not used to extract Wave-A components because Wave-A is observed in the upper end of vertical profiles. Instead, a linear background wind was subtracted from the profiles in the height region of 30–37 km using a least squares method, and a low-pass filter with a cutoff length of 4 km was applied to the vertical profiles of zonal and meridional winds at 1500 LST 11 May. The vertical profiles at 1800 and 2100 LST 11 May were not used for the wave analysis because of the contamination of the aforementioned cyclonic vortex situated near the observational site. Extracted profiles of zonal and meridional wind components are shown in Fig. 2.

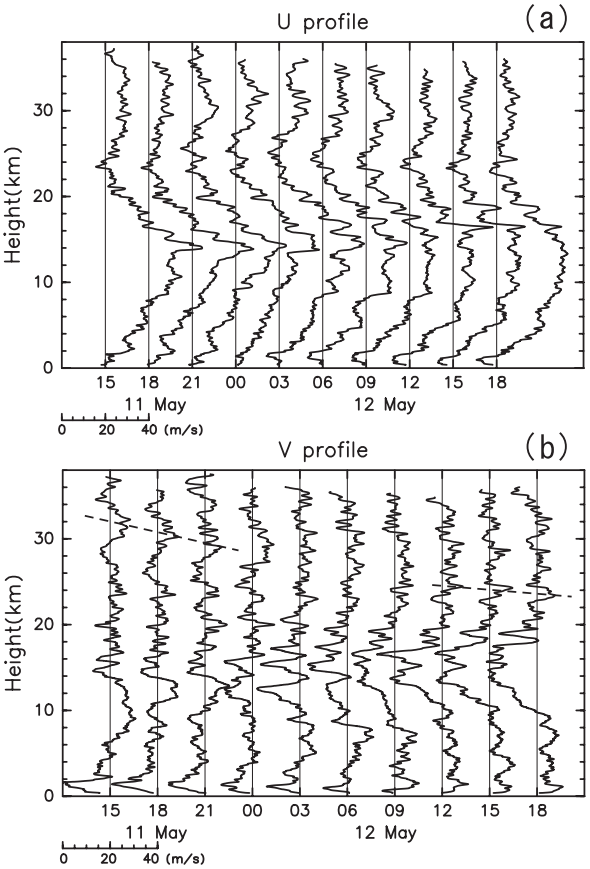

Fig. 1. Time series of vertical profiles of observed (a) zonal, and (b) meridional winds. Dashed lines trace phases of Wave-A and Wave-B, respectively.

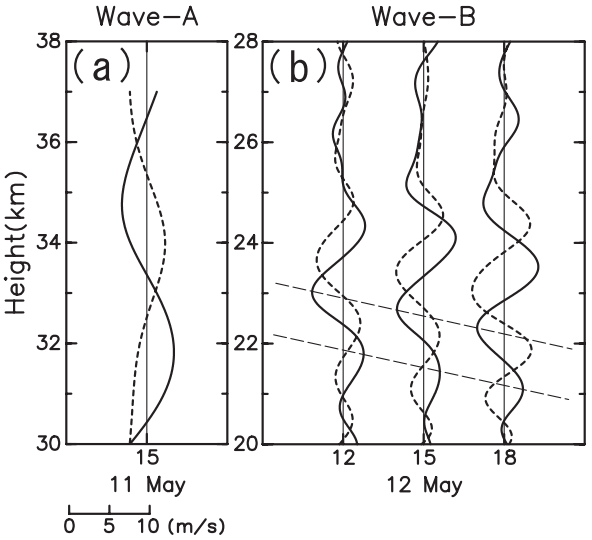

Fig. 2. Vertical profiles of (a) Wave-A and (b) Wave-B horizontal wind fluctuations. Dashed and solid curves show zonal and meridional wind components, respectively.

3. Hodograph analysis

A hodograph analysis method is useful to estimate gravity wave parameters from fine vertical profiles obtained by radiosondes, rockets and MST radars (e.g., Hirota and Niki 1986; Kitamura and Hirota 1989; Sato 1994). In this study, we applied this method to the Wave-A and Wave-B components assuming that they are due to IGWs.

According to the linear theory, the hodograph of an IGW has a shape of an ellipse. The direction of its major axis indicates that of wavenumber vector with an 180° ambiguity. The lengths of the major and minor axes of the hodograph ellipse correspond to the amplitudes of wind components parallel to ($\tilde{u}$) and perpendicular to ($\tilde{v}$) the wavenumber vector, respectively. The intrinsic frequency $\hat{\omega}$ can be determined from the polarization relation

$$\tilde{v} = -i\frac{f}{\hat{\omega}}\tilde{u}, \tag{1}$$

where f is the inertial frequency. The intrinsic frequency $\hat{\omega}$ is taken to be positive without losing any generality. The direction of vertical energy propagation of an IGW is estimated from the rotation of the hodograph ellipse: clockwise (anti-clockwise) rotation with height shows upward (downward) propagation in the Northern Hemisphere. The vertical wavelength of the IGW is also directly estimated from a cycle of the rotation.

Zonal (u') and meridional (v') wind fluctuations of Wave-A were fitted to sinusoidal functions using a least squares method as follows;

$$u' = \tilde{u}\cos\theta - \tilde{v}\sin\theta; \quad v' = \tilde{u}\sin\theta + \tilde{v}\cos\theta, \tag{2}$$

$$\tilde{u} = \hat{u}\sin\alpha; \quad \tilde{v} = \hat{v}\cos\alpha, \tag{3}$$

$$\alpha = mz + \varphi_0, \tag{4}$$

where $\hat{u}$ and $\hat{v}$ are the amplitude of $\tilde{u}$ and $\tilde{v}$, respectively, m is the vertical wavenumber, z is the height coordinate, φ_0 is constant, and θ is the angle between $\tilde{u}$ and the eastward direction.

The Wave-B zonal and meridional wind components were fitted similarly but we used $\alpha = mz - \omega t + \varphi_0$ instead of (4), where ω is the ground-based frequency and t is time. Thus, the values of ω as well as m are obtained directly from the fitting for Wave-B. On the other hand, only the value of m is directly estimated for Wave-A.

The other parameters are estimated using the dispersion relation of IGWs. The dispersion relation for the IGW in the uniform background fields under the Boussinesq approximation:

$$\hat{\omega}^2 = \frac{N^2(k^2+l^2)+f^2m^2}{k^2+l^2+m^2}, \tag{5}$$

where N, k and l are the Brunt–Väisälä frequency, zonal and meridional components of the horizontal wavenumber K ($K^2 \equiv k^2 + l^2$), respectively. For a hydrostatic IGW ($K^2 \ll m^2$) (5) is simplified as

$$\hat{\omega}^2 = f^2 + \frac{N^2K^2}{m^2}. \tag{6}$$

The horizontal wavelength is estimated using (6) for Wave-A and Wave-B. The value of N is about 2.2×10^{-2} s^{-1} which is estimated from radiosonde data in the middle stratosphere and f is 8.33×10^{-5} s^{-1} at the observation site.

The ground-based frequency ω is estimated using the Doppler relation

$$\omega = \hat{\omega} + UK, \tag{7}$$

using $\hat{\omega}$ from (1), K from (6) and the background horizontal wind U parallel to the horizontal wavenumber vector. It is worth noting that the estimation of ω using (7) is independent of the direct estimation from the phase variation in the time-height section as described in Section 2.

Figure 3 shows the hodograph of Wave-A components for the height region of 30–37 km. The abscissa and ordinate show the zonal and meridional wind components, respectively. Numerals near cross marks indicate heights at 1 km intervals.

The clockwise rotation with height suggests upward energy propagation. The vertical wavelength is about 6.0 km ($m = -1.0 \times 10^{-3}$ m^{-1}), and $\hat{\omega}$ and K are estimated from (1) and (6) at 1.7×10^{-4} rad s^{-1} (an intrinsic wave period of about 10 h) and 7.4×10^{-6} m^{-1} (a horizontal wavelength of about 850 km), respectively. Errors on respective wave parameters were estimated from the possible modification by the residual from the fitted ellipse for the ratio of the major and minor axes. The error of the horizontal wavelength is estimated as 30%. The other parameters of Wave-A have uncertainties of 20%.

The hodographs for Wave-B are shown in Fig. 4. The hodographs rotate clockwise with height, which indicates upward energy propagation similar to Wave-A. The vertical wavelength is about 2.6 km

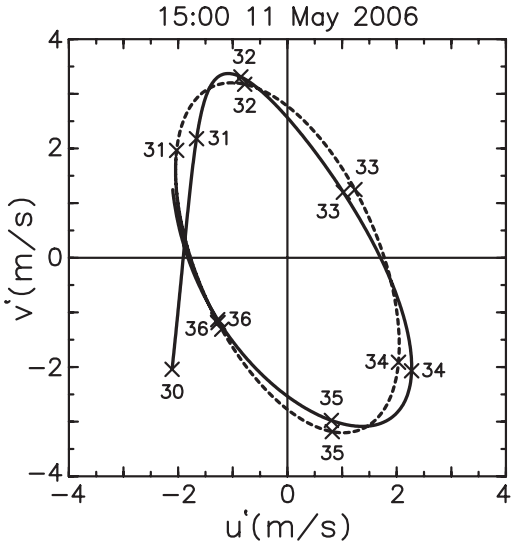

Fig. 3. A hodograph of the horizontal wind fluctuations of Wave-A in the height region from 30 to 37 km at 1500 LST 11 (solid curve) and a fitted ellipse (dashed curve). Numerals near cross marks indicate heights at 1 km intervals.

($m = -2.4 \times 10^{-3}$ m^{-1}), $\hat{\omega}$ and K are estimated from (1) and (6) at 1.0×10^{-4} rad s^{-1} (an intrinsic wave period of about 17 h) and 6.9×10^{-6} m^{-1} (a horizontal wavelength of about 900 km), respectively. The horizontal wavelength and k have uncertainty of 40%, and the other parameters have 20%.

Note that both Wave-A and Wave-B components have large amplitudes of about 4 m s^{-1}, which are adequate for meaningful analysis. The aspect ratio m/k of both Wave-A and Wave-B is larger than

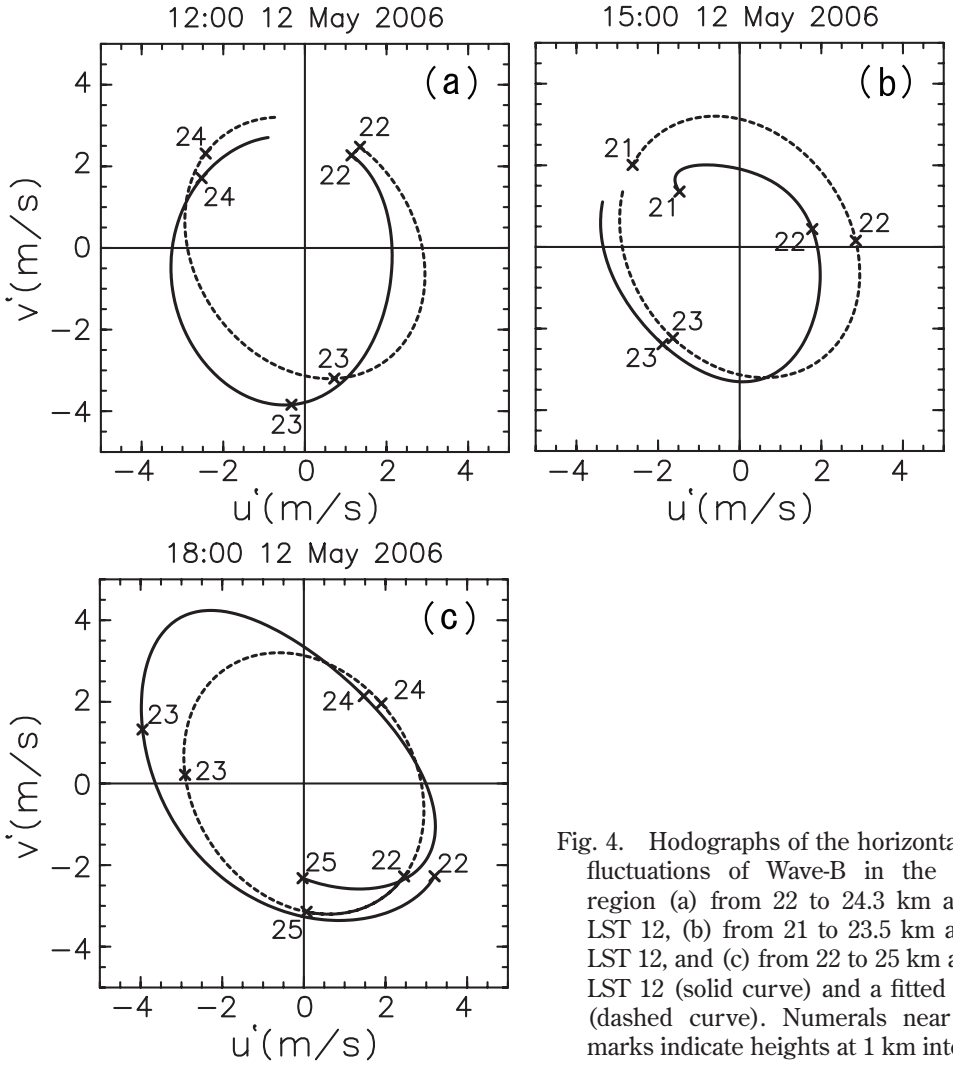

Fig. 4. Hodographs of the horizontal wind fluctuations of Wave-B in the height region (a) from 22 to 24.3 km at 1200 LST 12, (b) from 21 to 23.5 km at 1500 LST 12, and (c) from 22 to 25 km at 1800 LST 12 (solid curve) and a fitted ellipse (dashed curve). Numerals near cross marks indicate heights at 1 km intervals.

100, which is consistent with the assumption of the hydrostatic balance in (6).

The orientation of the major axis of the hodograph's ellipse in Figs. 3 and 4 indicates that both Wave-A and Wave-B propagate north-northwestward or south-southeastward. As shown by a ray tracing analysis in detail in Section 4, the ambiguity of 180° for the propagation direction disappears and it is confirmed that both waves likely propagate north-northwestward. In the case of north-northward propagation, (7) indicates that the ground-based horizontal phase speeds c are 23 m s^{-1} and 15 m s^{-1} with uncertainty of 30 %, and the ground-based wave frequencies are 1.6×10^{-4} rad s^{-1} (a ground-based wave period of about 11 h) and 8.3×10^{-5} rad s^{-1} (about 21 h) with uncertainty of 20% for Wave-A and Wave-B, respectively.

Note that the estimated ground-based wave period of Wave-A from (7) is consistent with the one estimated directly from the phase propagation seen in the time series (about 13 h). That of Wave-B also accords well with that estimated by the fitting analysis (about 17–24 h). This accordance validates the assumption that both Wave-A and Wave-B are due to IGWs. Table 1 summarizes the estimated wave parameters.

It is interesting that Wave-A and Wave-B structures are seen in the ECMWF data albeit the level is limited. Figure 5 is a map of horizontal divergence on 10 hPa at 1500 LST 11 when and where Wave-A was observed. Wave structure is clearly seen over Shigaraki. The horizontal wavelength of about 1000 km and phase alignments are consistent with the results of hodograph analysis. Note that our observation data is not included in the ECMWF operational analysis.

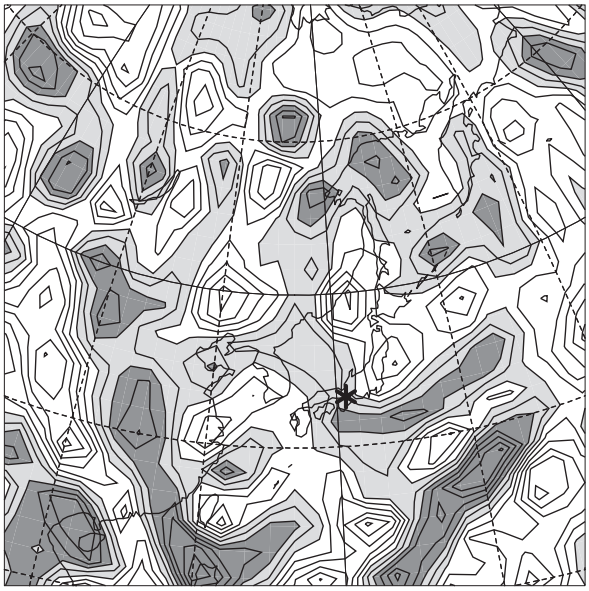

Fig. 5. Horizontal divergence on 10 hPa at 1500 LST 11 May 2006. Contour intervals are 2.5×10^{-6} s^{-1}. Negative regions are shaded. An asterisk (*) denotes the observation site.

4. Ray tracing analysis

a. Ray theory

A ray tracing analysis was made to elucidate sources of the IGWs using ray theory. A "ray" $\boldsymbol{X}(t)$ is defined as the trajectory of a wave packet moving at the local group velocity $\boldsymbol{C}_g$ depending on the wave parameters at the position $\boldsymbol{X}$ and t;

$$\frac{d_g \boldsymbol{X}(t)}{dt} = \boldsymbol{C}_g, \tag{8}$$

Table 1. The wave parameters of two IGWs estimated using a hodograph analysis.

	Wave-A	Wave-B
Observed time	1500 LST 11 May 2006	1200, 1500, 1800 LST 12 May 2006
Observed height	~34 km	~24 km
Vertical wavelength	6.0 km	2.6 km
Horizontal wavelength	850 km	900 km
Ground-based wave period	11 h	21 h
Vertical propagation	upward	upward
Horizontal propagation	North-northwestward	North-northwestward
Horizontal phase speed	23 m s^{-1}	15 m s^{-1}
Vertical flux of horizontal momentum	3.7×10^{-4} kg m^{-1} s^{-2}	7.8×10^{-4} kg m^{-1} s^{-2}

$$\boldsymbol{C}_g = (C_{gx}, C_{gy}, C_{gz}) \equiv \left(\frac{\partial \omega}{\partial k}, \frac{\partial \omega}{\partial l}, \frac{\partial \omega}{\partial m} \right), \tag{9}$$

where

$$\frac{d_g}{dt} \equiv \frac{\partial}{\partial t} + \boldsymbol{C}_g \cdot \nabla. \tag{10}$$

According to the ray theory (see Lighthill (1978) for details), the refraction of the wave vector along the ray is described as

$$\frac{d_g k}{dt} = -\frac{\partial \omega}{\partial x}, \quad \frac{d_g l}{dt} = -\frac{\partial \omega}{\partial y}, \quad \frac{d_g m}{dt} = -\frac{\partial \omega}{\partial z}, \tag{11}$$

under the WKB approximation. The Doppler relation (7) is rewritten using k, l, and the zonal ($\bar{u}$) and meridional ($\bar{v}$) components of the background wind as

$$\hat{\omega} = \omega - k\bar{u} - l\bar{v}. \tag{12}$$

Substituting (5) and (12) into (9) and (11), the group velocities and the temporal evolution of wavenumbers are expressed (Marks and Eckermann 1995) as

$$C_{gx} = \frac{k(N^2 - \hat{\omega}^2)}{\hat{\omega}(k^2 + l^2 + m^2)} + \bar{u}, \tag{13}$$

$$C_{gy} = \frac{l(N^2 - \hat{\omega}^2)}{\hat{\omega}(k^2 + l^2 + m^2)} + \bar{v}, \tag{14}$$

$$C_{gz} = \frac{m(f^2 - \hat{\omega}^2)}{\hat{\omega}(k^2 + l^2 + m^2)}, \tag{15}$$

$$\frac{d_g k}{dt} = -\frac{(k^2 + l^2)(N^2)_x}{2\hat{\omega}(k^2 + l^2 + m^2)} - k\bar{u}_x - l\bar{v}_x, \tag{16}$$

$$\frac{d_g l}{dt} = -\frac{(k^2 + l^2)(N^2)_y + 2m^2 f\beta}{2\hat{\omega}(k^2 + l^2 + m^2)} - k\bar{u}_y - l\bar{v}_y, \tag{17}$$

$$\frac{d_g m}{dt} = -\frac{(k^2 + l^2)(N^2)_z}{2\hat{\omega}(k^2 + l^2 + m^2)} - k\bar{u}_z - l\bar{v}_z. \tag{18}$$

Here we assume that the vertical component of the background wind is negligible. The rays of the IGWs are calculated by the backward integration using (8) and (13)–(15). At each time, $\hat{\omega}$ is obtained from (5) using k, l and m which are estimated from (16)–(18), and ω is calculated from (12).

The m and $\hat{\omega}$ values estimated by the hodograph analysis in the previous section were used as initial values. Background values of N^2, $\bar{u}$ and $\bar{v}$ where the wave packet was located were obtained from the ECMWF data by a cubic-spline interpolation method in time and by a linear interpolation method in latitude, longitude, and log-pressure vertical coordinates (Tomikawa and Sato 2005; Yamamori and Sato 2006). Initial locations were taken as heights of 34 km at 1500 LST 11 for Wave-A and of 24 km at 1500 LST 12 for Wave-B. The numerical integration was made using the fourth-order Runge-Kutta method with a constant time step of 30 min.

Following Marks and Eckermann (1995), we examined a parameter

$$\delta = \frac{1}{m^2}\left|\frac{dm}{dz}\right| \approx \frac{1}{m^2}\left|\frac{1}{C_{gz}}\frac{dm}{dt}\right|, \tag{19}$$

which should be small as long as the WKB assumption is valid, for the ray calculation at each time step. The integration is stopped when the δ value exceeds 10. This condition is usually met as $m \to 0$ ($\hat{\omega}^2 \to N^2$). In such situations, gravity waves would reflect vertically. Thus, vertical reflection is not expressed in our ray tracing calculation. The ray integration is also stopped when $\hat{\omega} < |f|$ or when $\hat{\omega} > N$.

b. Results of ray tracing analyses

Figures 6a and 6b show obtained ray paths projected onto longitude-latitude and longitude-height cross sections, respectively, in which the propagation directions are taken to be north-northwestward over Shigaraki for both waves. An interesting feature is that both ray paths are similar: the IGWs meandered mostly eastward around 200 hPa and 30°N, ascended rapidly to the south of Japan, and finally reached the observed levels over Shigaraki.

The conditions to stop the backward integration as described in Section 4a were not satisfied for a period of 10 days. Figure 7 shows the horizontal wind speed for 0300 LST 8, 9 and 10 May 2006 obtained using the ECMWF data. Asterisks denote the horizontal locations of wave packets for respecrtive snap shots. The mid-latitude westerly jet splits into two in the East Asia. It is found that the ray paths propagate along the southern flank of the jet having strong horizontal wind speeds greater than 20 m s^{-1}. The ray tracing analyses with a significantly reduced time step of 3 min were also

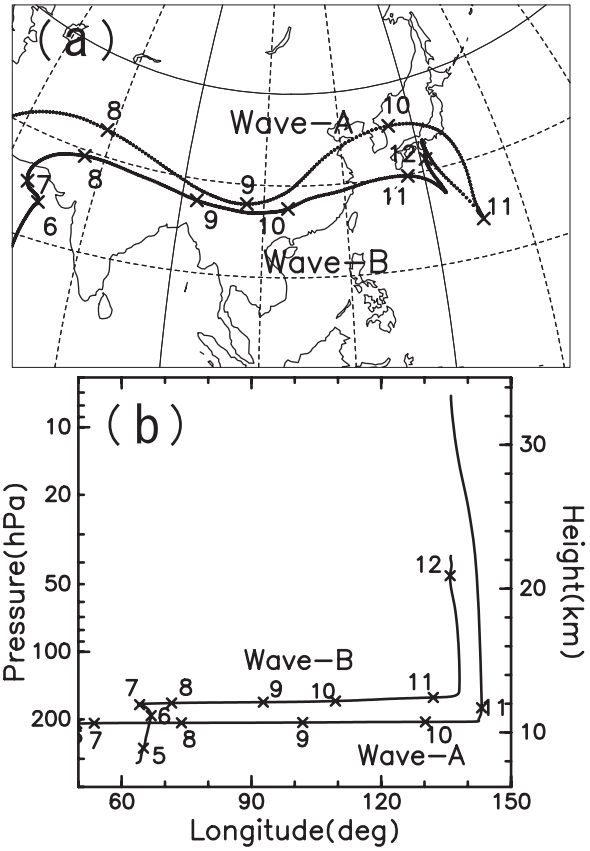

Fig. 6. The projection of rays traced for two IGWs (Wave-A and Wave-B) onto (a) longitudelatitude, and (b) longitude-height cross sections. Cross marks on the rays indicate the positions at 0000 LST of respective days.

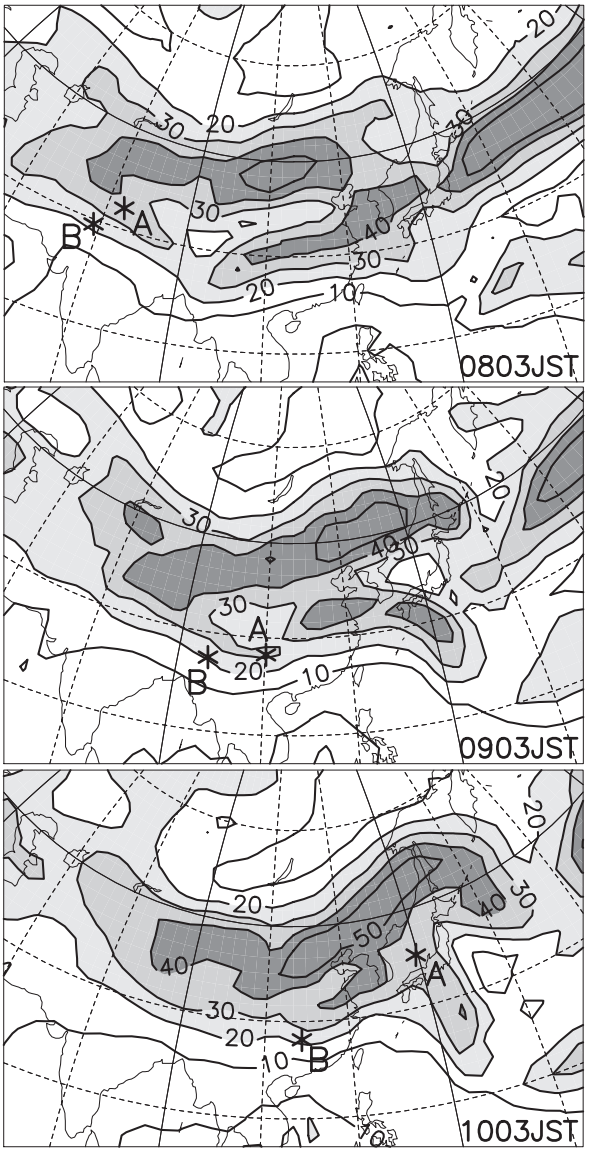

Fig. 7. A map of horizontal wind speed on 200 hPa at 0300 LST 8, 0300 LST 9 and 0300 LST 10 May 2006 obtained from ECMWF operational analysis data. Contour intervals are 10 m s^{-1}. Regions with stronger wind speeds are shaded more darkly. Asterisks denote the horizontal locations of IGW packets at each time.

made. The difference in the horizontal ray position was only less than 1° for both wave packets after a 5-day backward integration, indicating accuracy of the result of ray tracing analyses.

c. Generation mechanism

The spontaneous adjustment process is one of the important generation mechanisms of IGWs. Thus, we examine the distribution of the local Rossby number using the ECMWF data. The local Rossby number is a non-dimensional number describing departure from the geostrophic balance and defined as:

$$\mathrm{Ro}_\zeta \equiv |\zeta/f| \tag{20}$$

where ζ is the relative vorticity (Pedrosky 1987). Figure 8 shows a series of horizontal maps of Ro_ζ every 12 h at the pressure level where the IGW packets were located. A notable feature is that both wave packets propagate around the jet in the regions with large Ro_ζ values over a long period of about 5 days and are situated in small Ro_ζ regions

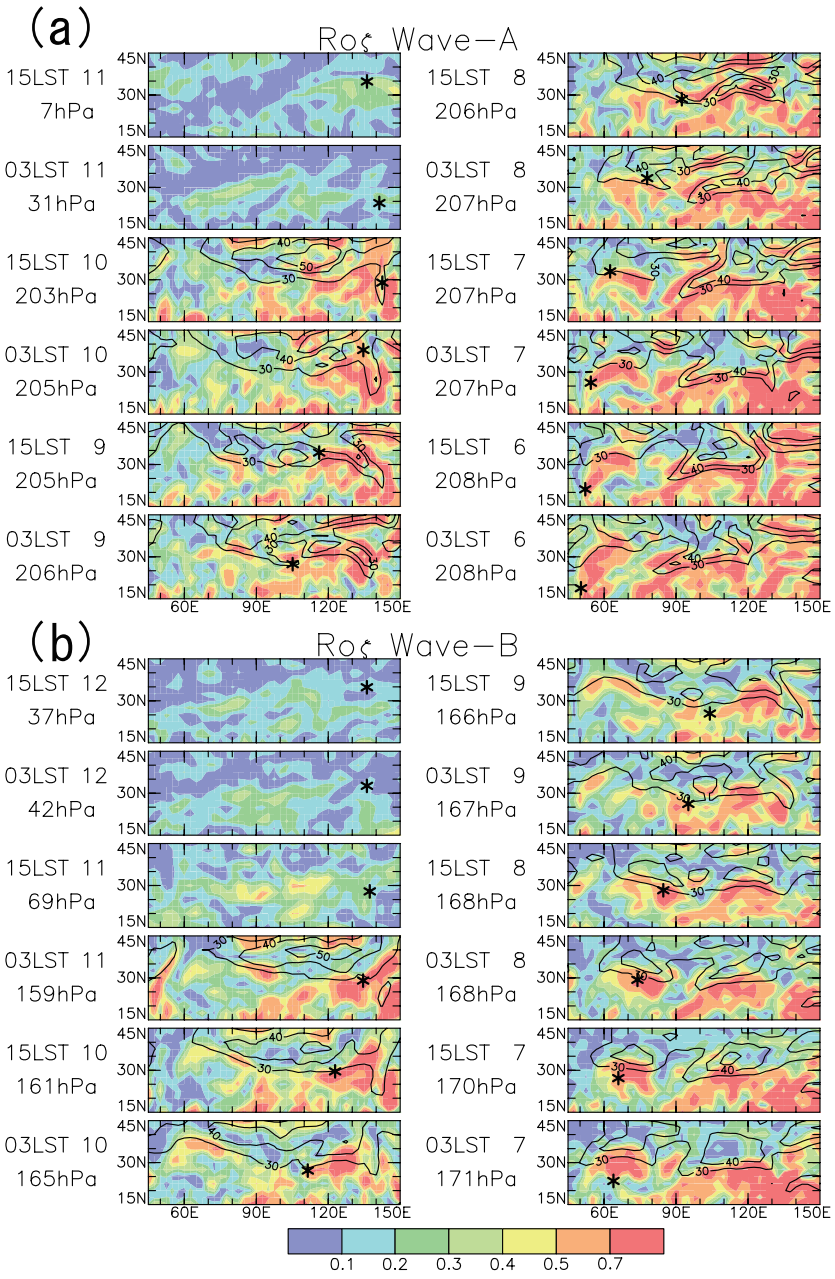

Fig. 8. A series of horizontal maps of local Rossby number every 12 h obtained from ECMWF operational analysis data at the pressure levels where the ray is located for (a) Wave-A, and (b) Wave-B. Asterisks denote the locations of IGW packets at each time. The abscissa and ordinate show longitude and latitude, respectively. Solid curves show wind speeds (> 30 m s^{-1}) with the intervals of 10 m s^{-1}.

while they ascend rapidly from the jet level just before they were observed at Shigaraki. It is noted that we cannot identify when the IGWs generated.

The cross-stream Lagrangian Rossby number is also an indicator of the unbalanced regions, which is introduced by Koch and Dorian (1988) and defined as:

$$\mathrm{Ro}_{\perp} = \frac{\left|\mathbf{V}_{\mathrm{ag}}^{\perp}\right|}{|\mathbf{V}|} \tag{21}$$

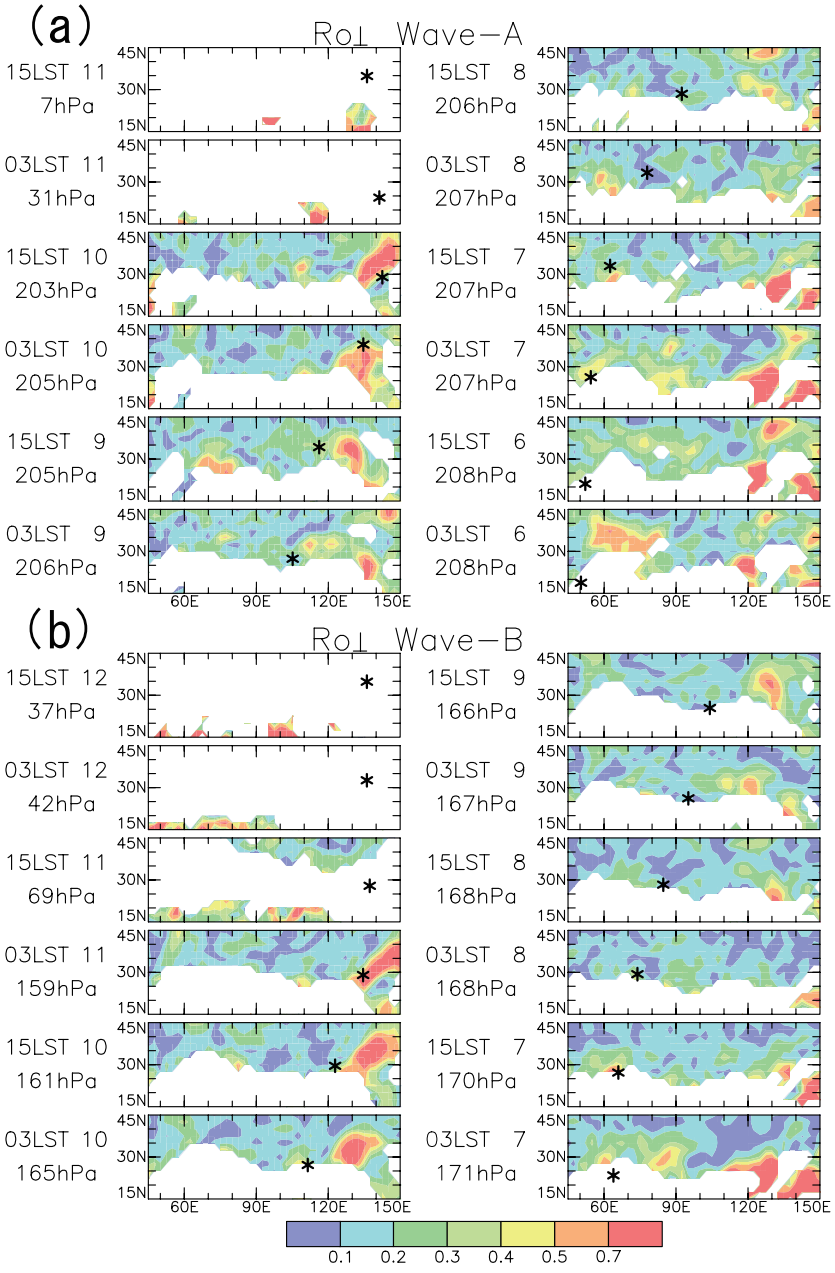

Fig. 9. Same as Fig. 8 but for the cross-stream Lagrangian Rossby number.

where $\mathbf{V}_{ag}^{\perp}$ shows the ageostrophic wind component perpendicular to the wind vector $\mathbf{V}$. Figure 9 shows horizontal maps of $Ro_{\perp}$. The values of $Ro_{\perp}$ in regions where $|\mathbf{V}| < 15$ m s^{-1} are not calculated because $Ro_{\perp}$ values may be spiriously large in such regions due to the small denominator. Significant $Ro_{\perp}$ values are observed in the regions where both wave packets are situated around the jet for about 2 days, although meaningful $Ro_{\perp}$ values were not obtained owing to small wind speeds on the 6th of May for Wave-A and before the 7th of May for Wave-B. This feature is consistent with the result of the Ro_{ζ} analysis.

Moreover, we also calculated the residual of the nonlinear balance equation (ΔNBE, e.g., Zhang et al. 2001) as another indicator of the unbalanced region:

$$\Delta\mathrm{NBE} = 2J(u,v) + f\zeta - \nabla^2\Phi - \beta u \qquad (22)$$

where $\beta = df/dy$ and Φ is the geopotential. However, ΔNBE may not be necessarily suitable to analyze the wave source when the grid size is large. In fact, for the present case, it seemed that the ΔNBE distribution obtained from the ECMWF data is messy and does not show meaningful signals (not shown). It is still controversial which is the best indicator of imbalance.

The ray paths may depend on the initial values of wave parameters. We examined the robustness by changing initial values in the estimated ranges for m and $\hat{\omega}$, ±1 h for time and ±500 m for height. However, resulting ray paths did not change largely (not shown).

The ray tracing analysis was also made when we assumed south-southeastward propagation for IGWs. Resulting ray paths varied greatly according to the initial values compared with the northnorthwestward propagation case. The ray paths were robust during the first 3 days, but any ray paths did not propagate in regions with large Ro_ζ and $\mathrm{Ro}_\perp$ values. Some rays lied in large Ro_ζ and $\mathrm{Ro}_\perp$ regions on 5 or more days before the initial date but only for a period shorter than 12 hours. It is inferred that large amplitudes of Wave-A and Wave-B are hardly achieved in such a short time period. Moreover, propagation for such a long time after wave generation may reduce the IGW amplitude due to dissipation.

Judged from the results of the ray tracing analysis, it is concluded that the horizontal propagation is north-northwestward for both IGWs, and confirmed that the generation mechanism is likely spontaneous adjustment around unbalanced flows.

5. Discussion

a. Possibilities of the other kinds of gravity wave sources

Although the topography, convection and shear instability are the other possible sources of gravity waves, it is shown that they are not likely in the following. First, topographically-forced gravity waves should have almost zero phase speeds, which is not the case for either Wave-A or Wave-B as estimated in Section 3. Second, gravity waves generated in association with convection tend to have shorter horizontal wavelengths than those (~1000 km) of Wave-A and Wave-B (e.g., Piani et al. 2000). Moreover, organized large-scale convective activities were not seen in the satellite images during the Wave-A and Wave-B events (not shown). Thus, convection and topographic effects are not likely as the IGW sources.

We also examined horizontal maps of Ri as in Fig. 8 (not shown). The Wave-B packet never lies in such low Ri regions during propagation around the jet. However, the ray of Wave-A is traced back in the vicinity of the regions where Ri is less than 3 at 1500 LST 09, 0300 LST 10 and 1500 LST 10. It is expected that small values of Ri are poorly expressed because vertical grid intervals of the ECMWF data are coarse. Thus, we cannot deny the possibility of the shear instability only from the Ri values at least for Wave-A.

Another notable feature for gravity waves generated by shear instability is that the ground-based horizontal phase speeds should be comparable to the mean wind at the unstable region (i.e., the intrinsic phase speed ($\hat{c} \equiv c - U$) is small; e.g., Fritts 1982, 1984)). Figures 10a and 10b show time series of $\hat{c}$, c and U, and those of the direction of K and the background wind, respectively, for Wave-A. In the time period of 1500 LST 9-1500 LST 10 May when the Wave-A packet is situated in the regions with small Ri, the intrinsic phase speed is large (about 10 m s^{-1}). Thus, the possibility of wave generation by the shear instability is also low for Wave-A.

Therefore, it can be concluded that the IGWs are generated in the vicinity of the unbalanced westerly jet through the spontaneous adjustment, although we can not identify when the IGWs are generated in such regions on the ray paths.

b. The horizontal directions of energy propagation

Sato (1994) made a statistical study of gravity waves over Shigaraki using the MU radar data over 3 years, which covers the altitude region up to about 22 km. It was shown that IGWs propagating westward relative to the mean wind were dominant in the height region of 18–22 km in winter, defined as October through May when a strong mid-latitude jet is situated. The characteristics are consistent with the topographically-forced gravity waves. On the other hand, in summer (June through September), the propagation direction was mostly northward in 18–22 km. The characteristics of the IGWs detected in the present study are consistent with those in summer. This is conceivable because the observation period corresponds to a transition period from winter to summer in the stratosphere

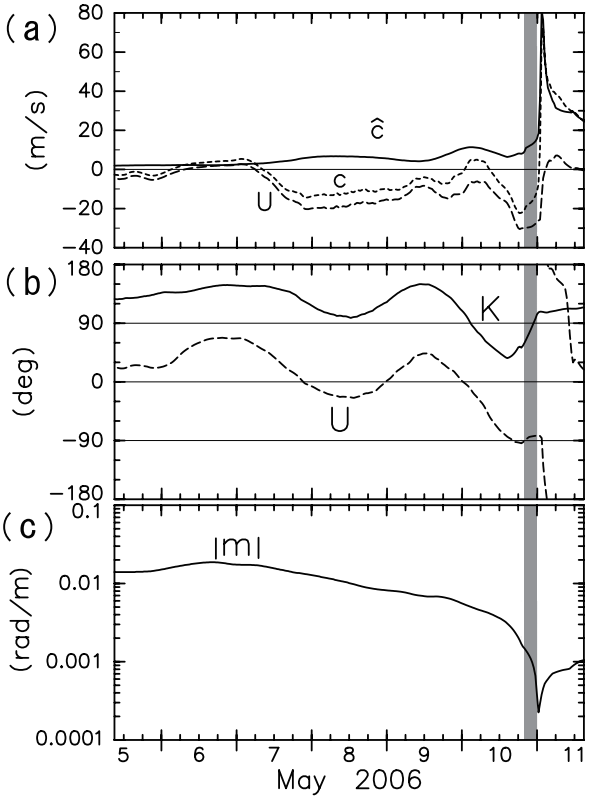

Fig. 10. Time variation of (a) the intrinsic horizontal phase speed $\hat{c}$ (solid curve), the groundbased horizontal phase speed c (dotted curve) and the background wind parallel to the horizontal wavenumber vector (dashed curves) U, (b) the direction of the horizontal wavenumber K (solid curve) and the background wind (dashed curve), and (c) the magnitude of the vertical wavenumber m of Wave-A. Shading indicates 2000 LST 10-0000 LST 11 May 2006 whenWave-A starts to ascend rapidly. Unit of the vertical axis in (b) is degree, north of east.

as shown in Section 2.

c. Sudden ascending from the jet level

An interesting feature observed in the results of the ray tracing analysis is that the IGWs ascended rapidly from the jet level slightly before they reached the observation site. We examine the reason why the vertical group velocity C_{gz} increased around 2100 LST 10 for Wave-A and around 0900 LST 11 for Wave-B.

Using the intrinsic horizontal phase speed $\hat{c}$, (15) can be rewritten as

$$C_{gz} = \frac{\sqrt{(\hat{c}^2 - \hat{c}_1^2)^3(\hat{c}_h^2 - \hat{c}^2)}}{\hat{c}(\hat{c}_h^2 - \hat{c}_1^2)}, \tag{23}$$

where $\hat{c}_h \equiv N/K$ and $\hat{c}_1 \equiv f/K$. For long-period IGWs such as Wave-A and Wave-B, $\hat{c}_h \gg \hat{c}$ because $\hat{\omega} \ll N$. Thus, (23) is approximated as

$$C_{gz} \approx \frac{\sqrt{(\hat{c}^2 - \hat{c}_1^2)^3}}{\hat{c}\hat{c}_h}. \tag{24}$$

This relation means that C_{gz} increases rapidly as $\hat{c}$ increases. For Wave-A, the direction of K (northward) is approximately the opposite of U direction (southward) in the jet-exit region around 2100 LST 10. It is considered that this is the reason why $\hat{c}$ and C_{gz} become large (see Fig. 6b, Fig. 7 and Fig. 10b). Figure 10c show time series of the magnitude of m. It is noted that the magnitude of m became small when Wave-A ascended rapidly. Similar results are obtained for the Wave-B case.

6. Summary and concluding remarks

We made intensive stratosphere observations using 10 radiosondes over 27 h of 11–12 May 2006 at Shigaraki, Japan (34.85°N, 136.11°E) with high accuracy and fine resolution. Balloons attained a maximum altitude of 36 km on average before bursting. Horizontal wind and temperature data were obtained in the wide height region including the middle stratosphere, which have rarely been analyzed except for rocket soundings and satellites whose resolution is not very high.

Characteristic wavelike fluctuations were observed around heights of both 34 km (Wave-A) and 24 km (Wave-B) and identified as the IGWs. Wave parameters of Wave-A and Wave-B are estimated by hodograph analysis. The ground-based wave periods are 11 and 21 h, the horizontal wavelengths are 850 and 900 km, and the vertical wavelengths are 6.0 and 2.6 km, for Wave-A and Wave-B, respectively. It is also shown that both of the IGWs propagate energy upward.

Next, we estimated sources of the IGWs by a ray tracing analysis. The results indicate that the ray paths of Wave-A and Wave-B have similar characteristics. The IGWs meandered eastward around 200 hPa and 30°N along the southern flank of the mid-latitude jet, turned north-northwestward and ascended rapidly where the background wind direction was changed to southward, and finally

reached the observed levels over Shigaraki. Interesting points is that a locally defined Rossby number and a cross-stream Lagrangian Rossby number are very large in the regions where the IGW packets were situated during propagation around the jet. In particular, both packets propagated large locally Rossby number regions over a long period of about 5 days. Therefore, it is likely that the IGWs were generated in the vicinity of the unbalanced westerly jet through the spontaneous adjustment processes.

It is considered that spontaneous emission of gravity waves as shown in the present study occurs ubiquitously in the atmosphere. Plougonven and Snyder (2005) investigated the propagation of IGWs radiated from the jet in the background flow having horizontal deformation and vertical shear. They showed that the background strongly influence the spatial distribution of the IGWs and the orientation of their wavenumber vector, which is called the "wave capture" mechanism. Further investigation on the detailed generation mechanism and characteristics of the emitted waves is needed. The use of realistic gravity-wave resolving global models would be promising to capture the role of spontaneously-emitted gravity waves in the atmosphere in a quantitative manner.

Acknowledgments.

The radiosonde observations were performed by Y. Tomikawa, K. Nishimura, T. Oyama and T. Kinoshita as well as the authors. We thank M. Yamamori for her kind advice for the ray tracing calculations. We also appreciate two anonymous reviewers for their valuable comments. European Centre for Medium-range Weather Forecasts operational data was used for the analyses. Figures were drawn using the GFD-DENNOU library.

References

Baldwin, M.P., L.J. Gray, T.J. Dunkerton, K. Hamilton, P.H. Haynes, W.J. Randel, J.R. Holton, M.J. Alexander, I. Hirota, T. Horinouchi, D.B. A. Jones, J.S. Kinnersley, C. Marquardt, K. Sato, and M. Takahashi, 2001: The Quasi-Biennial Oscillation. *Rev. Geophys.*, **39**, 179–229.

Fritts, D.C., 1982: Shear excitation of atmospheric gravity waves. *J. Atmos. Sci.*, **39**, 1936–1952.

Fritts, D.C., 1984: Shear excitation of atmospheric gravity waves. Part II: Nonlinear radiation from a free shear layer. *J. Atmos. Sci.*, **41**, 524–537.

Guest, F.M., M.J. Reeder, C.J. Marks, and D.J. Karoly, 2000: Inertia-gravity waves observed in the lower stratosphere over Macquarie Island. *J. Atmos. Sci.*, **57**, 737–752.

Haynes, P.H., C.J. Marks, M.E. McIntyre, T.G. Shepherd, and K.P. Shine, 1991: On the "downward control" of extratropical diabatic circulations by eddy-induced mean zonal forces. *J. Atmos. Sci.*, **48**, 651–678.

Hirota, I. and T. Niki, 1986: Inertia-gravity waves in the troposphere and stratosphere observed by the MU radar. *J. Meteor. Soc. Japan*, **64**, 995–999.

Kitamura, Y. and I. Hirota, 1989: Small-scale disturbances in the lower stratosphere revealed by daily rawinsonde observations. *J. Meteor. Soc. Japan*, **67**, 817–831.

Koch, S.E. and P.B. Dorian, 1988: A mesoscale gravity wave event observed during CCOPE. Part III: Wave environment and probable source mechanisms. *Mon. Wea. Rev.*, **116**, 2570–2592.

Lighthill, M.J., 1978: *Waves in Fluids*. Cambridge Univ. Press, 504 pp.

Marks, C.J. and S.D. Eckermann, 1995: A three-dimensional nonhydrostatic ray-tracing model for gravity waves: Formulation and preliminary results for the middle atmosphere. *J. Atmos. Sci.*, **52**, 1959–1984.

Oshima, R., 1997: Ray tracing analysis of gravity waves observed by the MU radar, M. Sc. thesis, Kyoto University, Japan, 29 pp. (Available from Department of Geophysics, Division of Earth and Planetary Sciences, Graduate School of Science Kyoto University, Kyoto 606-8502, JAPAN)

O'Sullivan, D. and T.J. Dunkerton, 1995: Generation of inertia-gravity waves in a simulated life cycle of baroclinic instability. *J. Atmos. Sci.*, **52**, 3695–3716.

Pedlosky, J., 1987: *Geophysical fluid dynamics*, Springer-Verlag, 710 pp.

Piani, C., D. Durran, M.J. Alexander, and J.R. Holton 2000: A numerical study of three-dimensional gravity waves triggered by deep tropical convection and their role in the dynamics of the QBO. *J. Atmos. Sci.*, **57**, 3689–3702.

Plougonven, R. and C. Snyder, 2005: Gravity waves excited by jets: Propagation versus generation. *Geophys. Res. Lett.*, **32**, L18802, doi:10.1029/2005 GL023730.

Plougonven, R. and C. Snyder, 2007: Inertia-gravity waves spontaneously generated by jets and fronts. Part I: Different baroclinic life cycles. *J. Atmos. Sci.*, **64**, 2502–2520.

Plumb, R.A., 2002: Stratospheric Transport. *J. Meteor. Soc. Japan*, **80**, 793–809.

Sato, K., 1994: A statistical study of the structure, saturation and sources of inertio-gravity waves in the lower stratosphere observed with the MU radar. *J. Atmos. Terr. Phys.*, **56**, 755–774.

Sato, K. and T.J. Dunkerton, 1997: Estimates of mo-

mentum flux associated with equatorial Kelvin and gravity waves. *J. Geophy. Res*., **102**, 26247–26261.

Sato, K. and M. Yoshiki, 2008: Gravity wave generation around the polar vortex in the stratosphere revealed by 3 hourly radiosonde observations at Syowa Station. *J. Atmos. Sci*., in press.

Sato, K., T. Kumakura, and M. Takahashi, 1999: Gravity waves appearing in a high-resolution GCM simulation. *J. Atmos. Sci*., **56**, 1005–1018.

Shibata, T., K. Sato, H. Kobayashi, M. Yabuki, and M. Shiobara, 2003: The Antarctic polar stratospheric clouds under the temperature perturbation by non-orographic inertia-gravity waves observed by micro pulse lidar. *J. Geophys. Res*., **108**, 4105, doi: 10.1029/2002JD002713.

Tomikawa, Y. and K. Sato, 2005: Design of the NIPR trajectory model. *Polar Met. Glaciol*., **19**, 120–137.

Uccelini, L. and S. Koch, 1987: The synoptic setting and possible energy sources for mesoscale wave disturbances. *Mon. Wea. Rev*., **115**, 721–729.

Watanabe, S., K. Sato, and M. Takahashi, 2006: A general circulation model study of orographic gravity waves over Antarctica excited by katabatic winds. *J. Geophys. Res*., **111**, D18104, doi:10.1029/2005JD006851.

Yamamori, M. and K. Sato, 2006: Characteristics of inertia gravity waves over the South Pacific as revealed by radiosonde observations. *J. Geophys. Res*., **111**, D16110, doi:10.1029/2005JD006861.

Yoshiki, M., N. Kizu, and K. Sato, 2004: Energy enhancements of gravity waves in the Antarctic lower stratosphere associated with variations in the polar vortex and tropospheric disturbances. *J. Geophys.Res*., **109**, D23104, doi:10.1029/2004JD004870.

Zhang, F., 2004: Generation of mesoscale gravity waves in upper-troposphere jet-front systems. *J. Atmos. Sci*., **61**, 440–457.

Zhang, F., S.E. Koch, C.A. Davis, and M.L. Kaplan, 2001: Wavelet analysis and the governing dynamicsof a large-amplitude mesoscale gravity-wave event along the East Coast of the United States. *Quart. J. Roy. Meteor. Soc*., **127**, 2209–2245.